PHYSICAL REVIEW APPLIED **3,** 064013 (2015)

Ablation of Submicrometer Holes Using an Extreme-Ultraviolet Laser

Andrew K. Rossall,[*] Valentin Aslanyan, and Greg J. Tallents
York Plasma Institute, University of York, Heslington, York YO10 5DD, United Kingdom

Ilya Kuznetsov, Jorge J. Rocca, and Carmen S. Menoni
Centre for Extreme Ultraviolet Science and Technology and Department of Electrical and Computer Engineering, Colorado State University, Fort Collins, Colorado 80523, USA

(Received 10 March 2015; published 19 June 2015)

Simulations and experiments are used to study extreme-ultraviolet (EUV) laser drilling of submicrometer holes. The ablation process is studied with a 2D Eulerian hydrodynamic code that includes bound-free absorption processes relevant to the interaction of EUV lasers with a solid material. Good agreement is observed between the simulated and measured ablated depths for on-target irradiances of up to 1×10^{10} W cm^{-2}. An increase in the irradiance to 1×10^{12} W cm^{-2} is predicted to ablate material to a depth of 3.8 μm from a single pulse with a hole diameter 3 to 4 times larger than the focal spot size. The model allows for the simulation of the interaction of a laser pulse with the crater created by a previous shot. Multiple-pulse lower-fluence irradiation configurations under optimized focusing conditions, i.e., approaching the diffraction limit, are shown to be advantageous for applications requiring mesoscale [(100 nm)–(1 μm)] features and a high level of control over the ablation profile.

DOI: 10.1103/PhysRevApplied.3.064013

I. INTRODUCTION

Considerable advances have been made in high-fluence extreme-ultraviolet (EUV) and x-ray laser technology as is shown by laser-plasma-based EUV lasers [1], free-electron lasers [2], and capillary discharge lasers [3–6]. With higher fluences and repetition rates up to 100 Hz [7] now available, EUV and x-ray lasers can be used to directly generate strongly coupled plasmas. Targets irradiated by EUV lasers are heated predominantly via direct photoionization, as opposed to inverse bremsstrahlung as with traditional optical infrared (IR) and ultraviolet (UV) lasers. This change in heating mechanism results in typically lower plasma temperatures and higher particle densities [8]. With traditional laser-produced plasmas, an expanding plume of plasma allows only absorption away from the target surface where the electron density drops below a critical value ($\simeq 10^{21}/\lambda_\mu^2$ cm^{-3}, where λ_μ is the laser wavelength in units of microns). By reducing the wavelength into the EUV to x-ray region, the critical electron density is typically greater than solid, and the laser photon energy E_p becomes sufficient to directly photoionize elemental components (ionization energy E_i), transferring energy ($E_p - E_i$) to the ejected electron. As the critical electron density (the point at which the real part of the dielectric function goes to zero) is typically higher than solid, the laser is able to penetrate the expanding plasma plume and continue to heat the solid material directly throughout the duration of the laser pulse. This increase in critical electron density differs from the interaction of optical IR and UV pulses with solids where the majority of the pulse energy is absorbed within the expanding plasma plume via inverse bremsstrahlung. Reducing the lasing wavelength to the EUV to soft-x-ray region also allows for a tighter focus due to a reduction in the diffraction limit. The tighter focus is a potentially desirable property for a number of applications, for example, mesoscale machining [9], mass spectrometry [10], and the coating of refractory material onto substrates.

To promote research and to accelerate the development of industrial applications, there is a significant motivation to produce compact and affordable EUV and x-ray laser sources for use in parallel with large-scale free-electron laser facilities such as the European free-electron laser, FLASH [11]. One such example is a table-top-size soft-x-ray laser system [12,13] based upon capillary discharge excitation of an Ar gas which causes lasing at 46.9 nm with a pulse energy up to 0.8 mJ [3,6] and a pulse length of 1.2 ns [4].

The work presented here utilizes a combination of fluid code modeling with atomic physics to simulate EUV and soft x-ray interaction with a solid, the laser energy deposition within the target, thermal energy transport, and the subsequent ablative flow away from the target. Using a 2D hydrodynamic code POLLUX [14–16] originally written to simulate optical and infrared-laser interaction and adding new absorption and atomic physics enables the simulation of the ablative properties of EUV and x-ray lasers. A comparison between simulation and experiment is shown for a capillary discharge laser operating at 46.9 nm ablating a planar parylene-N target under vacuum. Simulation results are then presented for higher irradiance and multiple-pulse interactions demonstrating the significant potential benefits of capillary discharge lasers for high-aspect-ratio hole drilling.

---

[*] andrew.rossall@york.ac.uk

II. POLLUX

The 2D Eulerian hydrodynamic code POLLUX originally written at the University of York was developed to model moderate-irradiance (10^9–10^{14} W cm^{-2}) optical- and infrared-laser irradiation of a solid target. With optical lasers, a strongly ionized plasma is produced which absorbs the incident laser beam. The code solves the three first-order quasilinear partial differential equations of hydrodynamic flow using the flux-corrected transport model of Boris and Book [17] with an upwind algorithm [18] for the first term. Energy absorption within the target is modified to include photoionization processes relevant to EUV and x-ray interactions. Energy is absorbed by the plasma electrons through inverse bremsstrahlung and direct photoionization and distributed via electron-ion collisions. The energy transfer rate between electrons and ions is calculated using the smaller value of the Spitzer electron collision frequency [19] or the electron-phonon collision frequency [20] in the low electron temperature (< 5 eV) regime and the Spitzer electron collision frequency for electron temperatures higher than 5 eV. For calculation of the equation-of-state (EOS) variables, POLLUX utilizes in-line hydrodynamic EOS subroutines from the CHART-D [21] equation-of-state package developed at Sandia National Laboratories and includes two phase transitions.

To properly calculate bound-free absorption processes within the target material, a model of atomic structure is used to account for transitions from both the ground and excited states. A superconfiguration model [22] is employed to reduce the number of levels to be considered. Ionization-dependent superconfigurations are calculated for an individual element by using the flexible atomic code (FAC) [23] to solve the radial wave function. The flexible atomic code provides detailed atomic structure, which is then postprocessed to form a reduced data set of ionization stages, atomic energy levels, and photoionization cross sections. As the produced plasma is close to solid density, the ionization energy E_i can be significantly lowered due to the presence of the surrounding electrons and ions. This ionization potential depression can cause pressure ionization, thus, reducing the absorption of the laser in that region. Ion potential depression is accounted for using a modified model originally developed by Stewart and Pyatt [24]. Ionic- and excited-state populations are determined by assuming local thermodynamic equilibrium and using the Saha-Boltzmann relation. Although the initial plasma state is highly nonequilibrated, it is shown that due to the high densities involved, the plasma ionization equilibrates on a time scale of tens of femtoseconds [25]. The fluid code simulations shown here operate on a hydrodynamic time scale of > 1 ps; therefore, the local thermodynamic equilibrium assumption is valid. An analytical approximation of the Kramers-Kronig relationship is used to determine temperature-dependent atomic scattering factors and, thus, the refractive index of the plasma, and has been reported previously [26]. This combination of atomic physics modeling of laser-absorption, EUV ray tracing within the plasma including a temperature-dependent refractive index and the simulation of the subsequent ablative flow from the target is a unique capability for the application of mesoscale machining.

III. EXPERIMENTAL BENCHMARKING

The benchmark simulation results shown here are for an Ar-based capillary discharge laser irradiating a planar parylene-N target, with a photon energy of 26.4 eV ($\lambda = 46.9$ nm), a FWHM pulse length of 1200 ps, and fluence ranging between 2 and 8 J cm^{-2}. Experimental measurements of the ablated depth in parylene-N are conducted using a capillary discharge laser system developed at Colorado State University [5].

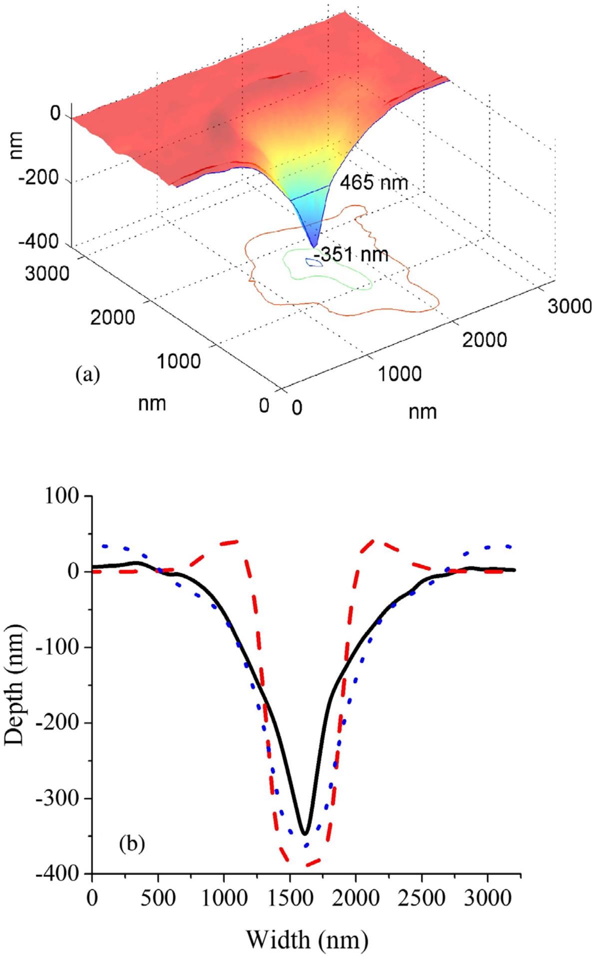

FIG. 1. (a) Experimentally obtained ablation profile. The FWHM and depth of the hole are indicated. The contours are cross sections of the ablated crater at 10%, 50%, and 90% of its depth. (b) Comparison with the simulated ablation profile for a fluence of 7.7 J cm^{-2} (6×10^9 W cm^{-2}). The black solid line in (b) is a lineout of the experimental profile in (a). Simulated ablation profiles are shown for a laser with a Gaussian beam profile (red dashed) and a double Gaussian approximation of the central lobe (containing 92% of total energy) and side lobe (containing 8% of the total energy) of an Airy disk (blue dotted).

The capillary discharge laser is focused under vacuum using a Fresnel zone plate with a numerical aperture of 0.12, where the smallest possible diameter of the first null of the Airy disk is approximately 240 nm. The spatial profile of the laser in the simulations is described by approximating the central lobe of the Airy disk as a Gaussian function. The diffraction-limited spot size in this case is a FWHM diameter of approximately 207 nm. In the experiments, craters with a FWHM diameter ranging between 650 and 850 nm are ablated.

By varying the fluence over the range tested via experimental measurement, a comparison can be made to ascertain the accuracy of the code in the simulation of EUV ablation. Figure 1(a) shows an image of an ablated parylene-N target measured using atomic-force microscopy after the shot for the fluence of 7.7 $\mathrm{J\,cm^{-2}}$. The corresponding lineout through the central ablated region is shown [Fig. 1(b)] with a comparison to two computed ablation profiles. The first using a Gaussian profile as described and the second using a double Gaussian profile to approximate an Airy pattern with 92% of the energy in the central lobe and 8% of the energy in a side lobe. Figure 2 shows a comparison between the ablated depth in parylene-N measured experimentally and the ablated depth predicted through simulation. The depth of ablation in the simulation is taken after 1300 ps ($t = 600$ ps is the peak of the pulse) at the point at which the ion temperature drops below the melting point, which for parylene-N is 0.06 eV (420 °C). The dashed lines indicate the resolution of the Eulerian mesh used in the simulations which is limited by the Courant-Friedrichs-Lewy condition [27].

Good agreement is observed between the ablated depth predicted via simulation and the experimentally observed ablated depth, giving confidence to the computational algorithms utilized. Current capillary discharge lasers are capable of pulse energies up to 0.8 mJ [6]; hence, irradiances approaching $1 \times 10^{12}\ \mathrm{W\,cm^{-2}}$ can be achieved with appropriate collection and focusing optics.

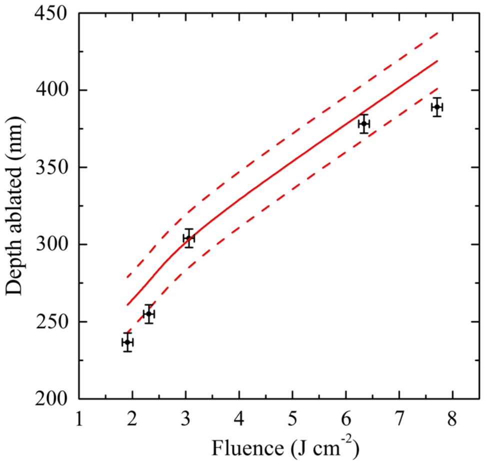

FIG. 2. Comparison between experimental ablated depth measurements (squares) and simulations (solid line) as a function of EUV laser fluence on target. The dashed lines indicate the resolution of the Eulerian mesh used in the simulations.

IV. SIMULATION RESULTS AND DISCUSSION

To explore the ablative capabilities of this technology, the effect of varying the irradiance from $1 \times 10^{9}\ \mathrm{W\,cm^{-2}}$ to $1 \times 10^{12}\ \mathrm{W\,cm^{-2}}$ is simulated, the results of which are shown in Fig. 3. Ablated depths of 3.8 μm per pulse are observed for the highest irradiance with a lateral hole size of 2.2 μm (FWHM) for a 0.5 μm diameter (FWHM) focal width. High-aspect-ratio submicron-size surface features are achievable, provided the system is optimized to inhibit lateral heat transport within the target. Figure 3 shows ablation profiles as a function of irradiance after 1300 ps of irradiation and demonstrates that lateral heat transport increases the feature size with increasing fluence as one would expect due to the increase in localized energy deposition in the target. Typical predicted temperatures for the laser-produced plasma range between a few electron volts for an on-target laser irradiance of $10^{9}\ \mathrm{W\,cm^{-2}}$ to 80 eV for $10^{12}\ \mathrm{W\,cm^{-2}}$ with plasma flow velocities along the laser axis ranging between 10^{5} and $10^{7}\ \mathrm{cm\,s^{-1}}$. Figure 4 shows the predicted on-laser axis plasma flow velocities and electron temperatures for irradiances of 10^{10}, 10^{11}, and $10^{12}\ \mathrm{W\,cm^{-2}}$.

Ablation with a laser operating in the EUV wavelength range optimizes energy deposition within the target. Parylene-N has > 70% transparency over the range of optical wavelengths, whereby photons at 46.9 nm have a penetration depth of only 20 nm in cold solid parylene-N. This short penetration depth leads to a highly localized deposition of energy in small volume, resulting in increased uniformity of heating and, thus, ablation. As the target

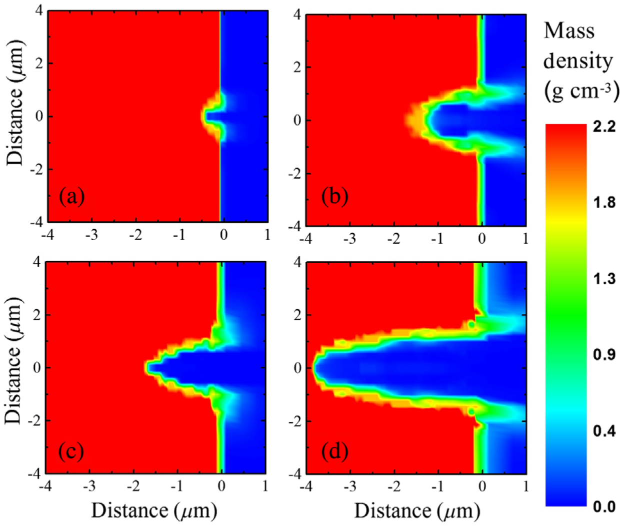

FIG. 3. Simulated ablation profiles at $t = 1300$ ps for (a) $1 \times 10^{9}\ \mathrm{W\,cm^{-2}}$, (b) $1 \times 10^{10}\ \mathrm{W\,cm^{-2}}$, (c) $1 \times 10^{11}\ \mathrm{W\,cm^{-2}}$, and (d) $1 \times 10^{12}\ \mathrm{W\,cm^{-2}}$ with a focal spot diameter of 500 nm.

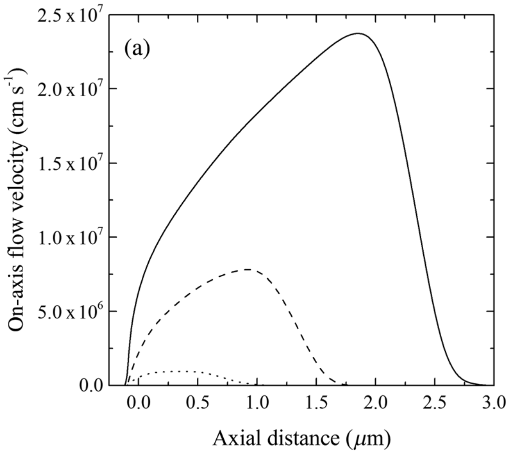

FIG. 4. On-laser axis plasma flow velocities (a) and electron temperatures (b) for irradiances of 1×10^{10} W cm^{-2} (dotted line), 1×10^{11} W cm^{-2} (dashed line), and 1×10^{12} W cm^{-2} (solid line) at the time of peak electron temperature $t = 10$ ps, after the start of the laser pulse.

material is heated via bound-free absorption dominated by the carbon component of the material, ionization increases, and the material becomes transparent as the 26.4-eV photon energy is only sufficient to ionize carbon to a C^{2+} state. This "bleaching" effect allows the EUV laser to ablate a significant amount of material in a single pulse, resulting in high-aspect-ratio drilling. Plasma refractive-index effects are found to be negligible for 26.4-eV photons in parylene-N for irradiances below 10^{10} W cm^{-2}. Above this irradiance, focusing and defocusing effects occur in different regions of the plasma, which in part contributes to the enlarging of the surface feature size. The additional heating due to the higher irradiance results in the dominant ionization stage in the plasma being C^{4+} or higher, and, thus, the free-electron density becomes comparable to the critical density of the EUV laser and further reduces the efficacy of the laser energy absorption. At lower irradiance, the dominant ionization stage is lower, the free-electron density remains subcritical, and the real component of the dielectric function remains greater than zero.

Over 85% of the ablation is seen to occur within the first half of the laser pulse for the parameters shown in Fig. 5, and as lateral heat transport dominates at later times, shortening the pulse length will inhibit the enlarging of the feature size by reducing the damaging thermal effects. Alternatively, multiple low-fluence pulses can be used to inhibit lateral heat transport, reducing the surface feature size and enabling high-aspect-ratio submicron-sized ablation. To enable multipulse simulation, a postprocessor is developed to configure the output of a single-pulse simulation. The postprocessor analyses output after the end of the first laser pulse, "removing" any plasma with a temperature greater than the melting point of parylene-N, i.e., resetting the temperature to room (0.025 eV) and the density to that of the vacuum ($10^{-7}\,\rho_{\text{solid}}$). The simulation is then restarted for a second pulse interacting with the existing ablation crater. Figure 6 indicates how a multiple-pulse technique can be utilized to ablate with high uniformity (approximately constant width over ablated depth) and improved surface feature size. Figures 5(a) and 5(b) show the ablation profiles after one and four pulses, respectively, with a focal spot diameter (FWHM) of 500 nm and an irradiance of 5×10^9 W cm^{-2}. After four pulses, a depth of 4.2 μm is ablated with a lateral hole size of 1.3 μm (FWHM). This hole size will reduce further as the diffraction limit is approached, as shown in Figs. 5(c) and 5(d). Figures 5(c) and 5(d) show the ablation profiles for a beam of the same irradiance with a focal spot diameter of 200 nm after one and two pulses, respectively. An ablated depth of 2.4 μm is observed after two pulses, with a lateral hole size of 644 nm (FWHM). This aspect ratio indicates the potential of EUV-laser ablation for sub-micron-size hole drilling under optimized focusing conditions. Using the computational environment described above, the ablative

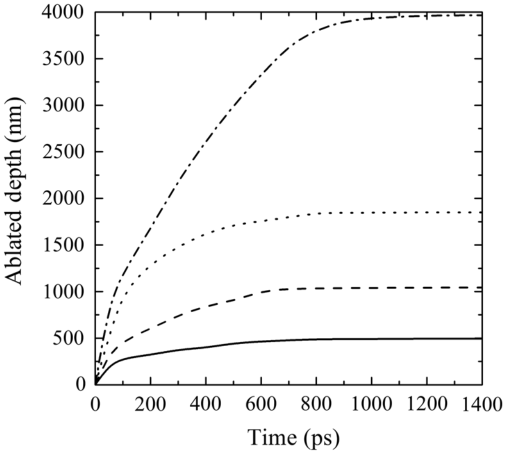

FIG. 5. Simulated ablated depth per pulse as a function of time and irradiance for 1×10^9 W cm^{-2} (solid), 1×10^{10} W cm^{-2} (dashed), 1×10^{11} W cm^{-2} (dotted), and 1×10^{12} W cm^{-2} (dash-dot). The pulse length is 1200 ps, and the focal spot diameter is 500 nm.

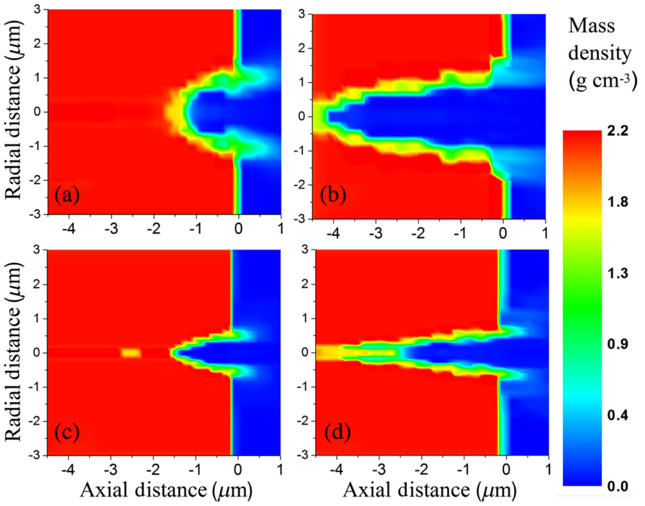

FIG. 6. Simulated ablation profiles at $t = 1300$ ps with an irradiance of 5×10^9 W cm^{-2} for focal spot diameters of 500 nm after (a) one pulse and (b) four pulses, and 200 nm after (c) one pulse and (d) two pulses.

characteristics can be readily optimized depending upon the requirements of the application.

V. CONCLUSION

This work demonstrates how a fluid code combined with relevant atomic physics is used to simulate the heating and subsequent ablation induced by a capillary discharge laser with a photon energy of 26.4 eV. Good agreement is observed between the ablated depth measured experimentally and the predicted depth obtained via simulation for on-target irradiances of up to 6×10^9 W cm^{-2}. Increasing the irradiance in the simulation to 1×10^{12} W cm^{-2} shows an increase in surface feature size due to lateral heat transport. Over 85% of the ablation occurs within the first half of the 1200-ps laser pulse and lateral heat transport increases at later time increasing the surface feature size further. Multiple lower-fluence pulses under optimized focusing conditions will be advantageous for applications requiring high-aspect-ratio mesoscale [(100 nm)–(1 μm)] features and a high level of control over the ablation profile.

ACKNOWLEDGMENTS

This work is funded by EPSRC Grant No. EP/J019402/1. J. J. R. acknowledges the support of NSF Grant No. PHY1004295. All data created during this research are available by request from the University of York Data Catalogue.

[1] G. J. Tallents, The physics of soft x-ray lasers pumped by electron collisions in laser plasmas, J. Phys. D **36**, R259 (2003).

[2] B. W. J. McNeil and N. R. Thompson, X-ray free-electron lasers, Nat. Photonics **4**, 814 (2010).

[3] J. J. Rocca, E. C. Hammarsten, E. Jankowska, J. Filevich, M. C. Marconi, S. Moon, and V. N. Shlyaptsev, Application of extremely compact capillary discharge soft x-ray lasers to dense plasma diagnostics, Phys. Plasmas **10**, 2031 (2003).

[4] B. R. Benware, C. D. Macchietto, C. H. Moreno, and J. J. Rocca, Demonstration of a High Average Power Tabletop Soft X-Ray Laser, Phys. Rev. Lett. **81**, 5804 (1998).

[5] S. Heinbuch, M. Grisham, D. Martz, and J. J. Rocca, Demonstration of a desk-top size high repetition rate soft x-ray laser, Opt. Express **13**, 4050 (2005).

[6] C. D. Macchietto, B. R. Benware, and J. J. Rocca, Generation of millijoule-level soft-x-ray laser pulses at a 4-Hz repetition rate in a highly saturated tabletop capillary discharge amplifier, Opt. Lett. **24**, 1115 (1999).

[7] B. A. Reagan, W. Li, L. Urbanski, K. A. Wernsing, C. Salsbury, C. Baumgarten, M. C. Marconi, C. S. Menoni, and J. J. Rocca, Hour-long continuous operation of a tabletop soft x-ray laser at 50–100 Hz repetition rate, Opt. Express **21**, 28380 (2013).

[8] M. Berrill, F. Brizuela, B. Langdon, H. Bravo, C. S. Menoni, and J. J. Rocca, Warm photoionized plasmas created by soft-x-ray laser irradiation of solid targets, J. Opt. Soc. Am. B **25**, B32 (2008).

[9] H. Bravo, B. T. Szapiro, P. W. Wachulak, M. C. Marconi, W. Chao, E. H. Anderson, C. S. Menoni, and J. J. Rocca, Demonstration of nanomachining with focused extreme ultraviolet laser beams, IEEE J. Sel. Top. Quantum Electron. **18**, 443 (2012).

[10] J. -W. Shin, F. Dong, M. E. Grisham, J. J. Rocca, and E. R. Bernstein, Extreme ultraviolet photoionization of aldoses and ketoses, Chem. Phys. Lett. **506**, 161 (2011).

[11] K. Tiedtke *et al.*, The soft x-ray free-electron laser FLASH at DESY: Beamlines, diagnostics and end-stations, New J. Phys. **11**, 023029 (2009).

[12] J. J. Rocca, V. Shlyaptsev, F. G. Tomasel, O. D. Cortázar, D. Hartshorn, and J. L. A. Chilla, Demonstration of a Discharge Pumped Table-Top Soft-X-Ray Laser, Phys. Rev. Lett. **73**, 2192 (1994).

[13] J. J. Rocca, F. G. Tomasel, M. C. Marconi, V. N. Shlyaptsev, J. L. A. Chilla, B. T. Szapiro, and G. Giudice, Discharge-pumped soft-x-ray laser in neon-like argon, Phys. Plasmas **2**, 2547 (1995).

[14] G. J. Pert, Two-dimensional hydrodynamic models of laser-produced plasmas, J. Plasma Phys. **41**, 263 (1989).

[15] G. J. Pert, Quasi-Lagrangian rezoning of fluid codes maintaining an orthogonal mesh, J. Comput. Phys. **49**, 1 (1983).

[16] A. K. Rossall, V. Aslanyan, and G. J. Tallents, in *SPIE Optical Engineering+Applications*, edited by A. Klisnick and C. S. Menoni (International Society for Optics and Photonics, Washington, 2013), pp. 884912–9.

[17] J. Boris and D. Book, Flux-corrected transport. III. Minimal-error FCT algorithms, J. Comput. Phys. **20**, 397 (1976).

[18] R. Courant, E. Isaacson, and M. Rees, On the solution of nonlinear hyperbolic differential equations by finite differences, Commun. Pure Appl. Math. **5**, 243 (1952).

[19] L. Spitzer and R. Härm, Transport phenomena in a completely ionized gas, Phys. Rev. **89**, 977 (1953).

[20] O. Peyrusse, Coupling of detailed configuration kinetics and hydrodynamics in materials submitted to x-ray free-electron-laser irradiation, Phys. Rev. E **86**, 036403 (2012).

[21] S. L. Thompson, Sandia National Laboratories Report No. SC-RR-70-2, 1970.

[22] S. B. Hansen, J. Bauche, and C. Bauche-Arnoult, Superconfiguration widths and their effects on atomic models, High Energy Density Phys. **7**, 27 (2011).

[23] M. F. Gu, The flexible atomic code, Can. J. Phys. **86**, 675 (2008).

[24] T. R. Preston, S. M. Vinko, O. Ciricosta, H.-K. Chung, R. W. Lee, and J. S. Wark, The effects of ionization potential depression on the spectra emitted by hot dense aluminium plasmas, High Energy Density Phys. **9**, 258 (2013).

[25] V. Aslanyan and G. J. Tallents, Local thermodynamic equilibrium in rapidly heated high energy density plasmas, Phys. Plasmas **21**, 062702 (2014).

[26] A. K. Rossall and G. J. Tallents, Generation of warm dense matter using an argon based capillary discharge laser, High Energy Density Phys. **15**, 67 (2015).

[27] R. Courant, K. Friedrichs, and H. Lewy, On the partial difference equations of mathematical physics, IBM J. Res. Dev. **11**, 215 (1967).